Time-lapse resistivity imaging: CSEM-data 3-D double-difference inversion and application to the Reykjanes geothermal field

François Bretaudeau, Frédéric Dubois, S-G Bissavetsy Kassa, Nicolas Coppo, Pierre Wawrzyniak, Mathieu Darnet

submitted to *Geophys. J. Int.*

Time-lapse resistivity imaging : CSEM-data 3D double-difference inversion and application to the Reykjanes geothermal field

F. Bretaudeau*, F. Dubois, S-G. Bissavetsy Kassa, N. Coppo, P. Wawrzyniak, M. Darnet

BRGM, 3 Av. Claude Guillemin, Orléans 45060, France

SUMMARY

Time-lapse resistivity tomography bring valuable information on the physical changes occurring inside a geological reservoir. In this study, resistivity monitoring from CSEM data is investigated through synthetic and real data. We present three different schemes currently used to perform time-lapse inversions and compare these three methods: parallel, sequential and double difference. We demonstrate on synthetic tests that double difference scheme is the best way to perform time-lapse inversion when the survey parameters are fixed between the different time-lapse acquisitions. We show that double difference inversion allows to remove the imprint of correlated noise distortions, static shifts, and most of the non-linearity of the inversion process including numerical noise and acquisition footprint. It also appears that this approach is robust against the baseline resistivity model quality, and even a rough starting resistivity model built from borehole logs or basic geological knowledge can be sufficient to map the time-lapse changes at their right positions. We perform these comparisons with real land time-lapse CSEM data acquired one year apart over the Reykjanes geothermal field.

Key words: Controlled-Source Electromagnetics, time-lapse inversion, double-difference inversion, geothermal monitoring, resistivity variations

1 INTRODUCTION

Geophysical imaging allows to recover the physical parameters of geological reservoirs. Geological reservoirs can be exploited for various economic reasons: oil and gas production, power and heat generation from geothermal energy, C02 storage or water supply management. All those reservoirs change over time along with their physical parameters. Time-lapse geophysical imaging is a perfect opportunity to monitor changes occurring inside the reservoirs. It consists in carrying out at different time a geophysical acquisition over a same region, and produce a structural image showing the temporal changes between the two acquisitions. The first acquisition is generally called baseline and the following acquisitions are considered as monitors.

Electromagnetic methods are well suited for time-lapse imaging as shown by several successful applications and promising works (e.g., Miller et al. 2008; Peacock et al. 2013; Rosas-Carbajal et al. 2015; Tietze et al. 2015; Abdelfettah et al. 2018; Patzer 2019). For diffusive methods (e.g., Controlled-Source EM (CSEM), magnetotellurics (MT), time-domain EM, DC Electric Resistivity Tomography (ERT)), the inversion of the baseline and monitor data sets are usually performed separately, then the difference between the two inverted models is presented as the time-lapse variation in resistivity of the reservoir. This scheme is called a parallel inversion. The high non-linearity and non-uniqueness of the resistivity imaging problems make the inversion results still strongly dependent of the path taken by the inversion. This effect may be exacerbated in presence of high level of noise, which can result in very different inverted models, even without significant model changes. At the end, the time-lapse image may reflect different inversion paths but not necessarily structural time-lapse differences.

To overcome some problems of parallel inversions, different time-lapse inversion schemes have been proposed. Sequential inversion is one of the common alternative where the monitor data are inverted starting from the inverted baseline model (Wirianto et al. 2010; Asnaashari et al. 2014). In this approach, hypothesis on small time-lapse signals are considered and thus reduced the non-linearity by starting inversion of the monitor data from the resistivity model obtained by the baseline data inversion which is supposed to be already close to the final result. However, the monitor data inversion can be influenced by parts of the data that remain unexplained by the baseline inversion. This may hamper the proper reconstruction of the time-lapse image, with little or none information on resistivity changes over time. An alternative technique is proposed by Karaoulis et al. (2011), they make use of regularization in time to control the consistency of the different models and slice their data set in different time-steps. This approach which is in essence a constrained parallel inversion framework may be interesting when many time-steps are available and if the inversion runs fast enough to perform

⋆ email: f.bretaudeau@brgm.fr

several inversions simultaneously. It is rarely the case for most 3-D ERT, CSEM or MT problems for which computing resources are usually an issue (e.g., Commer & Newman 2008; Puzyrev et al. 2016; Shantsev et al. 2017). It is noteworthy that parallel inversion drawbacks can also be mitigated by constraining the inversion of the time-lapse data set using the result of the baseline inversion as a prior model. Although the method is still poorly constrained, the idea behind prior constraints is the same as the time-regularization of Karaoulis et al. (2011), in which a similarity between the time-lapse models is imposed. Parallel and sequential inversion are the only possible approaches if the baseline and monitor acquisitions have different geometries and recording parameters between the baseline and the monitor acquisitions.

For common-acquisition setup between surveys (same geometry, same acquisition parameters), an alternative inversion technique is available to obtain more stable results by reducing the effect of noise and non-linearity of the inversion process. This scheme called double difference or differential inversion is based on the combination of baseline and monitor data. This concept is largely used in global seismology to remove common biases between data for a same acquisition (e.g., Kuo et al. 1987; Houser et al. 2008). Asnaashari et al. (2014) applied the double difference scheme to time-lapse FWI problems. A first baseline inversion can be computed and this model is used as starting model for the monitor inversion. But, unlike the sequential inversion, inverted data are a composite data made from the differences between monitor and baseline data. Double difference inversion is common in medical imaging (e.g., De Donno & Cardarelli 2017), in seismic travel-time tomography (Ajo-Franklin et al. 2007), was used for 4-D seismic reflection by (Tao et al. 2013) with a stochastic inversion approach, and was investigated on seismic full-waveform inversion by Asnaashari et al. (2014) and Zhang & Huang (2013). To our knowledge, its use for resistivity monitoring is not reported yet, and a rigorous comparison with the various possible time-lapse inversion strategies still needs to be performed. In this study, we work within the framework of the 3-D frequency domain CSEM, but all the results and conclusions are also valid for other resistivity methods such as MT, time-domain EM, DC electric resistivity tomography. Most of the conclusions can be directly transposed to other geophysical monitoring problems involving an iterative linear or nonlinear inverse problem.

We present and compare three different time-lapse schemes: parallel, sequential, and double difference inversion, in a similar way than in Asnaashari et al. (2014). We first present and study the advantages of each method, and compare their behaviors using synthetic 3-D CSEM data inversion over simple models. We then apply those schemes on a real land CSEM data example. Those data are composed of a baseline and a monitor data set acquired at one year of interval on the Reykjanes geothermal field in Iceland (Darnet et al. 2018). We show that double difference strategy brings a substantial advantage for time-lapse monitoring over the others methods.

2 TIME-LAPSE INVERSION STRATEGIES

In this part, we describe the main features of the three time-lapse inversion strategies: parallel, sequential and double difference inversion schemes. Though the theory behind time-lapse inversion is rather simple, knowing the theoretical differences can be worthy (e.g., Miller et al. 2008; Routh et al. 2012; Asnaashari et al. 2014). Data-fitting procedures are usually used to solve the resistivity inversions. These inversions are intrinsically non-linear, and iterative optimization methods have to be employed. For each iteration k, we try to minimized the data residual vector which is typically defined as the difference between observed data and data calculated in the current model $\mathbf{m_k}$:

$$\delta \mathbf{d_k} = \mathbf{d_{obs}} - \mathbf{d_{cal}}(\mathbf{m_k}) \tag{1}$$

with the computed data $\mathbf{d_{cal}}$ related to the resistivity model $\mathbf{m_k}$ by the forward operator $\mathbf{G}$:

$$\mathbf{d_{cal}}(\mathbf{m_k}) = \mathbf{G}(\mathbf{m_k}). \tag{2}$$

We define two different data sets corresponding to a baseline acquisition ($\mathbf{d_{obs1}}$) and a monitor acquisition ($\mathbf{d_{obs2}}$). First, a baseline reconstruction needs to be done by minimizing the difference between $\mathbf{d_{obs1}}$ and $\mathbf{d_{cal}}$ generated in a $\mathbf{m_0}$ starting model. However, at the end of this first inversion, discrepancies remain between observed and predicted data coming from our inability to properly build the true resistivity model. This can be due to a poor data coverage, to inaccurate forward modelling, insufficient spatial description of the model due to coarse grid parameterization for the inverse problem, high regularization or simply to the resolution limits of the geophysical method as well as the existence of local minima in the inversion process. We note this first difference $\delta \mathbf{d_{m_0}}$. Another contribution comes from noise which affects data. We can further decompose this noise into two contributions: uncorrelated and correlated noise between acquisitions and will be denoted as $\mathbf{d_{noise}}$ and $\mathbf{d_{static}}$, respectively. An additional input will appear for the monitor data due to the time-lapse signal related to resistivity changes, $\mathbf{d_{pert}}$. These contributions can be summarized into the two following equations:

$$\mathbf{d_{obs1}} = \mathbf{d_{m_0}} + \delta \mathbf{d_{m_0}} + \mathbf{d_{static}} + \mathbf{d_{noise_1}} \tag{3}$$

$$\mathbf{d_{obs2}} = \mathbf{d_{m_0}} + \delta \mathbf{d_{m_0}} + \mathbf{d_{static}} + \mathbf{d_{noise_2}} + \mathbf{d_{pert}}. \tag{4}$$

Lets consider the three main possibilities of time-lapse inversion. It is important to keep in mind that the first schemes namely *parallel* and *sequential* inversions do not necessarily need to have the exact geometry setup between the baseline and the monitor acquisition, even though it is usually preferable. Although, it seems to be an advantage compared to the *double difference* strategy, we will show that this constrain is balanced by other significant advantages. First, we are going to start with a quick description of *parallel* and *sequential* inversion (Figure 1). In case of *parallel* scheme, baseline and monitor inversions are completely decoupled. We compute the time-lapse image by taking the dif-

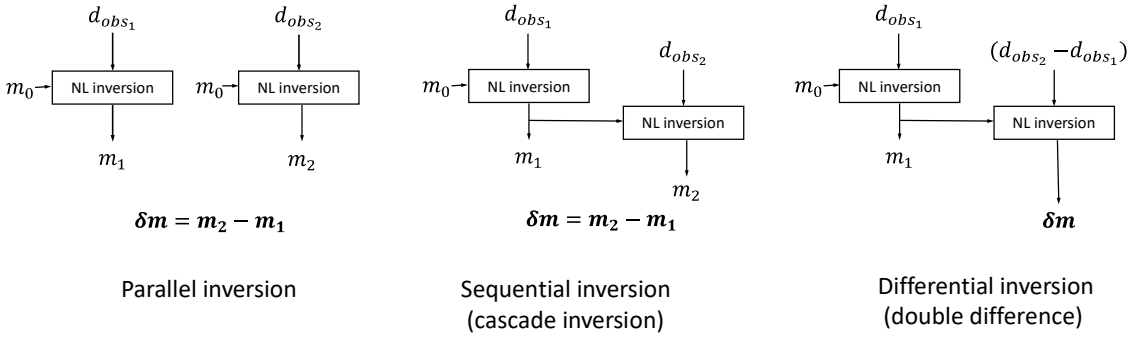

Figure 1. Parallel, sequential and differential inversion frameworks for time-lapse imaging. m_0 is the starting model, $\mathbf{d_{obs_1}}$ and $\mathbf{d_{obs_2}}$ are the baseline and monitor data, $\mathbf{m_1}$ and $\mathbf{m_2}$ the baseline and monitor models. Usage of $\mathbf{m_1}$ as a starting model for the double difference inversion is possible but other options are possible.

ference between the final inverted models. As previously said, baseline and monitor data set do not need to have the same geometry (number of data, number of receivers/sources). This seemingly advantage is a potential pitfall for inversion tuning. We are going to compare images with potentially different inverting mesh, regularization parameters and thus very different local resolution. This will induce signals in the time-lapse model mainly related to the resolution difference between baseline and monitor inversion. Besides, the inverse problem is highly non-linear which implies complex noise propagation between data and model estimates. Surely, noise propagation can be quite different between baseline and monitor inversion, and considering the same random noise between the two data set ($\mathbf{d_{noise_1}} = \mathbf{d_{noise_2}}$) may be far to be true. Moreover, both baseline and monitor inversion are biased by the static noise $\mathbf{d_{static}}$.

If *sequential* strategy is used, the baseline data $\mathbf{d_{obs_1}}$ lead to the baseline model $\mathbf{m_1}$ which explains the data and include an error $\delta\mathbf{m_1}$ due to unexplained parts of the data, lack of resolution, bad coverage, coarse parameterization, regularization, and noise $\mathbf{d_{noise_1}}$ and $\mathbf{d_{static}}$. Then the monitor data $\mathbf{d_{obs_2}}$ are inverted by using the baseline model $\mathbf{m_1}$ as starting model. According to equations (1) and (4), the data residual at first iteration is:

$$\begin{aligned}
\delta\mathbf{d_2}^{seq} &= \mathbf{d_{obs2}} - \mathbf{d_{cal}}(\mathbf{m_1}) \\
&= (\mathbf{d_{m_1}} + \delta\mathbf{d_{m_1}} + \mathbf{d_{static}} + \mathbf{d_{noise_2}} + \mathbf{d_{pert}}) - \mathbf{d_{m_1}} \\
&= \mathbf{d_{pert}} + \delta\mathbf{d_{m_1}} + \mathbf{d_{static}} + \mathbf{d_{noise_2}}. \qquad (5)
\end{aligned}$$

Equation (5) shows that the data residual is still containing contributions from modelling errors $\delta\mathbf{d_{m_1}}$ and noise beside the time-lapse signal. If the baseline model is imperfectly reconstructed, $\delta\mathbf{d_{m_1}}$ may be significant and the monitor inversion will not focus exclusively on the time-lapse signal $\delta\mathbf{d_{pert}}$. If the unexplained part of the baseline data is higher than the time-lapse signal, the resulting model

difference $\mathbf{m_2} - \mathbf{m_1}$ may highlight locations where baseline is far from the true resistivity model instead of resistivity changes between the two acquisitions.

In *double difference inversion*, extra care should be taken on the perfectly match between baseline and monitor data set geometry. Though it could seem to be a limit of the method, it is probably the best for highly repeatable surveys in geophysics. First, the baseline is reconstructed exactly as in parallel or sequential inversion (left/middle schematic on figure 1). However, in the second step instead of inverting the monitor data we invert the data difference (Asnaashari et al. 2014). We thus define data difference as $\mathbf{\Delta d} = (\mathbf{d_{obs_2}} - \mathbf{d_{obs_1}})$. Then, we rewrite the data residual vector at an iteration k as:

$$\delta \mathbf{d_2}^{dble} = (\mathbf{d_{obs_2}} - \mathbf{d_{obs_1}}) - (\mathbf{d_{cal}}(\mathbf{m_k}) - \mathbf{d_{cal}}(\mathbf{m_1})) \tag{6}$$

In order to use exactly the same inversion algorithm as for the baseline inversion, we can build a composite observed dataset:

$$\mathbf{d_{comp}} = \mathbf{d_{obs_2}} - \mathbf{d_{obs_1}} + \mathbf{d_{cal}}(\mathbf{m_1}) \tag{7}$$

to obtain the following data residual:

$$\delta \mathbf{d_2}^{dble} = \mathbf{d_{comp}} - \mathbf{d_{cal}}(\mathbf{m_k}). \tag{8}$$

At the first iteration, starting from the baseline model $\mathbf{m_1}$, this data residual results in:

$$\begin{aligned} \delta \mathbf{d_2}^{dble} &= (\mathbf{d_{obs_2}} - \mathbf{d_{obs_1}} + \mathbf{d_{cal}}(\mathbf{m_1})) - \mathbf{d_{cal}}(\mathbf{m_1}) \\ &= \mathbf{d_{pert}} + (\mathbf{d_{noise_2}} - \mathbf{d_{noise_1}}). \end{aligned} \tag{9}$$

A very interesting feature of this approach is illustrated by equation (9) with comparison to equation (5). The data residual is not anymore dependent on the error of baseline reconstruction $\delta \mathbf{d_{m_1}}$, making the inversion much more robust against the starting model, numerical modeling inaccuracies and non-linearity of the inversion. This is extremely important because of the non-uniqueness of EM inverse problem. Furthermore, the double difference allows interesting possibilities such as inverting time-lapse data without necessity to reconstruct accurate baseline model, which can be in some cases a very tough task. The baseline model can therefore be constructed using a different technique, for instance using borehole resistivity logs, geological knowledge, or by coupling the baseline data with any other prior data only available for the baseline. A typical interesting possibility is to use very dense acquisition layout to build a good baseline model and keep a reduced common layout for monitoring that would be sufficient to image the time-lapse variations. Another interesting behavior is the robustness against noise. In sequential inversion, $\mathbf{d_{noise_1}}$ and $\mathbf{d_{static}}$ both affect the reconstruction of $\mathbf{m_1}$, then $\delta \mathbf{d_{m_1}}$ and $\mathbf{d_{noise_2}}$ and $\mathbf{d_{static}}$ affect the reconstruction of $\mathbf{m_2}$. For double difference inversion, only $\mathbf{d_{noise_2}} - \mathbf{d_{noise_1}}$ is present in the residual, which means that coherent noise between the two

data sets is completely removed. EM surveys are often strongly affected by coherent noise such as anthropogenic noise or galvanic distortion effects (static shift), resulting sometimes in very challenging inversions and poor data fits that easily cause sequential inversion to fail. Such static-shift effects are totally removed in the data difference, it enables to invert without any kind of hazardous static-shift corrections even if the baseline reconstruction fails. As a consequence only time-lapse changes are highlighted and artefacts such as static shifts and coherent noises are removed. Besides, the double difference inversion does not require inversion code modifications, and can even be applied using a commercial or code-protected inversion software with no additional implementation effort. Additionally, the approach can still be combined with prior constrains (Asnaashari et al. 2014) to focus the inversion on specific zones of the model or if necessary with the time-regularization approach of Karaoulis et al. (2011).

3 MODELING AND INVERSION METHODOLOGY

In the following, we are making use of a 3D frequency-domain CSEM and MT modeling and inversion code named POLYEM3D (Bretaudeau et al. 2016). Electric and magnetic fields are computed in the frequency domain by using the secondary-field approach (e.g., Streich 2009). In the secondary-field approach, the electromagnetic field is split into two contributions. A first part, called 'primary field', is computed using a semi-analytical formulation for any kind of source in an 1-D layered background. Then, the 'secondary field' is computed numerically by finite-difference of the Helmholtz equation such as

$$\nabla \times \nabla \times \mathbf{E^S} \; + \; j\omega\mu_0 \boldsymbol{\sigma} \mathbf{E^S} \;\; = \;\; -j\omega\mu_0(\boldsymbol{\sigma} - \boldsymbol{\sigma}_\mathrm{P})\mathbf{E^P} \tag{10}$$

where $\mathbf{E^P}$ and $\mathbf{E^S}$ are respectively the primary and the secondary electric fields, $\boldsymbol{\sigma}$ the 3-D resistivity vector, μ_0 the magnetic permeability, ω the angular pulsation and $\boldsymbol{\sigma}_\mathrm{P}$ the resistivity vector in the reference 1-D model where $\mathbf{E^P}$ is calculated. Equation (10) is discretized using a finite-volume approach on an irregular cartesian staggered grid scheme (e.g., Streich 2009), resulting in the following linear system

$$\mathbf{A}(\omega, \boldsymbol{\sigma}) \; \mathbf{E^S} \;\; = \;\; \mathbf{b}(\mathbf{E^P}, \boldsymbol{\sigma} - \boldsymbol{\sigma_p}, \omega). \tag{11}$$

Equation (11) is solved using a massively parallel direct solver such as MUMPS (Amestoy et al. 2001, 2019) or WSMP (Gupta et al. 2001). Then, computed data ($\mathbf{d_{cal}}$) at every receiver locations r, for a source s, and a frequency ω are extracted from the total electric field $\mathbf{E^{Tot}} = \mathbf{E^P} + \mathbf{E^S}$ using the rigorous interpolator of Shantsev & Maaø (2015).

$$\mathbf{d_{cal}}^{r,s,\omega}(\boldsymbol{\sigma}) = R^{r,c} \, \mathbf{E^{Tot}}(\omega, \boldsymbol{\sigma}) \tag{12}$$

with $R^{r,c}$ a linear mapping operator. It typically includes 3-D interpolators, curl operator to get magnetic fields, and any change of variables required by the user.

Once predicted data ($\mathbf{d_{cal}}$) are computed for a starting model, a data-fitting misfit function f is defined in order to quantify the information extracted from observed data ($\mathbf{d_{obs}}$). This misfit function can be written as

$$f = \frac{1}{2}(\mathbf{d_{obs}} - \mathbf{d_{cal}})^{\dagger}\mathbf{W_d}^{\dagger}\mathbf{W_d}(\mathbf{d_{obs}} - \mathbf{d_{cal}}). \tag{13}$$

by using the euclidian norm and $\mathbf{W_d}$ the diagonal weighting matrix typically containing the inverse data covariances. For each iteration, minimization of the misfit function is carried out to obtain a model update $\mathbf{\Delta m_k}$. Then the new model at the iteration $k+1$ is computed as

$$\mathbf{m_{k+1}} = \mathbf{m_k} + \alpha_k \, \mathbf{\Delta m_k}, \tag{14}$$

where α_k is the step length at the iteration k.

The POLYEM3D code offers several optimization algorithms to compute $\mathbf{\Delta m_k}$ and the step length α_k. Preconditioned gradient-based algorithm such as steepest descent and l-BFGS based on Métivier & Brossier (2016) are available and require only the computation of the predicted data, misfit, and the gradient of the misfit function at each iteration (e.g., Nocedal & Wright 2006). Gauss-Newton inversion using LSQR (Paige & Saunders (1982)) is also available, it requires in addition the explicit computation and storage of the Fréchet derivative matrix, which is possible because of the use of a direct solver for the forward and adjoint modelling (e.g., Operto et al. 2009; Grayver et al. 2013; Shantsev et al. 2017). Those algorithms have slightly different computational performances, but also have different convergence properties which can have a significant impact on the final model due to the high non linearity of the inverse problem. All those algorithms also rely on an efficient line-search based on a bracketing approach such as described in Nocedal & Wright (2006) and Métivier & Brossier (2016), where the Wolfe conditions must be satisfied at each iteration. Various changes of variables, grid change operators, re-parameterization tools, data misfit formulations and regularisation tools are also available but their description is out of the scope of this paper.

4 TIME-LAPSE ON SYNTHETIC EXAMPLES

4.1 Parallel, sequential and double-difference

To compare the behavior of parallel, sequential and double-difference inversion, we design a simple example. The baseline is defined as a 1-D model composed of 4 layers. It includes a 50 m thick $10\,\Omega.m$ conductive reservoir located at 400m depth bellow two more resistive layers ($50\,\Omega.m$ and $100\,\Omega.m$) and above a $200\,\Omega.m$ background. As time-lapse targets, we build a monitor model where we add to

this baseline a small rectangular volume of $200\times600\times45$m at $40\,\Omega.m$ symbolizing a resistive anomaly embedded in the conductive reservoir, and a conductive rectangular volume of $200 \times 500 \times 85$m at $20\,\Omega.m$ inside the $100\,\Omega.m$ layer. The monitor model and the setup are illustrated figure 2. First examples are computed without noise in data, then realistic noise will be added to our modelings to better visualize the benefits of the double-difference strategy.

The modeling grid is made of 25 m cubes in the zone of interest (core domain). This zone lays over an area of $1000\times2400\times600\,m$ and is extended with a 1.5 factor outward of the core domain. The total grid is composed of 300.000 cells and includes the air layer. A regular grid of 121 stations is positioned over the zone of interest with 100 m between each station. For completeness sake, the all setup along with the modeling grid is displayed on figure A1. The horizontal electric components are recorded at each receiver position. Two pairs of two orthogonal galvanic point sources are placed at 1200 m from the middle of the model on each side of the receiver grid. The seven following frequencies are computed and inverted [10 Hz, 20 Hz, 40 Hz, 80 Hz, 125 Hz, 300 Hz, 600 Hz].
For the inversion, a coarser grid made of cubic splines is defined. Lateral and vertical nodes for the inversion grid are represented by squares on figure A2. It is restricted to the core domain and limited to 600 m depth. The inversion grid is built on a basis of cubic B-splines and composed of $11 \times 11 \times 8$ cells with increasing size vertically and constant size horizontally. This coarse parameterization using smooth interpolations allows implicit regularization and thus ensures similar smoothness of the solutions for all the tests presented here and prevent the inversion from a potential dependency on an arbitrary tuning of regularization hyperparameters. The choice of the coarse parameterization of the inverse problem here may not be optimal for the reconstruction of a 'blocky' model, but as everything is kept unchanged during all the synthetic experiments, it does not change the conclusion of the study. Moreover, this choice will enhance the difference of behavior that may be due to the non-uniqueness of the solutions. To quantify differences between two synthetic data sets, we define the total relative RMS error as:

$$RMS = \sqrt{\frac{\sum_i (d_{obs_i} - d_{cal_i})^* W_{d_i} W_{d_i} (d_{obs_i} - d_{cal_i})}{\sum_i d^*_{obs_i} W_{d_i} W_{d_i} d_{obs_i}}}. \tag{15}$$

The error of the forward modelling can be estimated by comparing numerical and analytical solutions in the 1-D baseline model. The total RMS error in the synthetic model is estimated to less than 0.2%. The time-lapse response can be also quantified as RMS difference between the monitor and the 1-D baseline: it is estimated to 2.06%. It is thus larger than the forward modeling accuracy, and is also close but higher than a typical 1% CSEM measurement repeatability error (Darnet et al. 2018; Tietze et al. 2019). However, the typical coarse parameterization and the low resolution of the EM method

	Starting model		Baseline	Parallel Monitor	Sequential Monitor	Differential (start 2,06%)
3D inversion from m0=homo	RMS baseline RMS monitor	17,21% 17,20%	6,47% 25 it	7,47% 17 it	6,43% 12 it	1,17% 18 it
3D inversion from m0=smooth1d	RMS baseline RMS monitor	45,86% 45,57%	5,35% 17 it	5,50% 17 it	5,03% 12 it	1,17% 18 it
m0 = homo – no baseline inversion						1,72% 11 it
m0 = exact 1D baseline						0,24% 65 it

	Starting model		Baseline	Parallel Monitor	Sequential Monitor	Differential (start 2,89%)
3D inversion of noisy data from m0=homo	RMS baseline RMS monitor	21,44% 21,45%	15,10% 11	15,10% 11	15,10% Fail	2,28% 24 it

Table 1. Synthesis of RMS data residuals before and after inversion.

does not allow to fit the data to a RMS error lower than 5%. The starting and final RMS error of each inversion tests presented in this paper are summarized in the table of figure 4.1.

In a first step, the baseline and the monitor data are inverted separately starting from an $50\,\Omega.m$ homogeneous background. The true model is displayed on figures 2a). The inverted baseline and monitor resistivity models are represented on figures 2b) and 2c). The 1-D layered structure is globally reconstructed with the low resolution inherent to EM methods. The reservoir and the resistive layer above the reservoir are too thin to be resolved so the final models are clearly equivalent models that integrate several layers. As a consequence, the resistivity contrasts of each layer are underestimated. However baseline and monitor data inversion both reach respectively a RMS of 6.47% and 7.47%. An example of baseline data fit is depicted figure 3 for the dominant electric field component of a station located in the middle of the survey in an in-line configuration. The example shows a good fit on both amplitude and phase on the whole spectrum with in accuracy of the order of the time-lapse signal. In the monitor model, the conductive and resistive rectangle anomalies are both visible approximately at their right position, but the contrasts are underestimated. The difference between those two models results in the *parallel* time-lapse resistivity model presented figure 4b). The targets are visible but slightly mislocated vertically, and significant variations also appear everywhere in the rest of the model. In particular, the deep structure also show more than $20\,\Omega.m$ variations.

In a second step, we perform a sequential inversion by inverting the monitor data starting from the baseline model. The sequential monitor model (figure 2d) looks similar to the parallel monitor model

and gives a final RMS error of 6.43% slightly lower that the parallel inversion. However, the sequential time-lapse model of figure 4c shows that even though the anomalies are imaged, the model also includes several inconsistent high amplitude resistivity variations, in particular in the shallow part, and the anomalies seems to be smoothed outside of their right position. Those artefacts are due to a part of the baseline data which had not been explained in the baseline model and are partially explained during the second step of inversion.

Finally we build a composite data and apply an double-difference inversion starting again from the inverted baseline model. The double difference monitor model is presented figure 2e and the differential time-lapse model figure 4d. Even though the conductive target is still spreaded vertically, the differential model is clearly less affected by artefacts. The amplitudes of the perturbations are weaker than in the parallel and sequential models but the anomalies are more compact, closer to their right positions and there is almost no artefacts in the rest of the model. Data are very well fitted by the double difference inversion, reducing the RMS from 2.06% to 1.17%. The data fit is illustrated figure 5 for the same station that in figure 3. The weighted time-lapse response in black is mostly explained (fit the red curve). In this figure, we also see in blue dots that the unexplained residuals of the baseline inversion is at the level of the time-lapse signal. That means that even though the baseline model used is not perfectly reconstructed with a RMS residual much higher that the time-lapse response, the time-lapse signal is well explained here, which is not the case for parallel and sequential inversion where it is not possible to know which part of time-lapse and/or baseline signal is explained.

4.2 Robustness with starting model and baseline

In order to assess the starting model quality, we also performed different inversions with various starting models. A smoothed version of the true 1-D layered model is used (Figure 6a). The fit of the baseline and monitor is improved (45.57% to 5.35%). The parallel difference model is significantly improved, which illustrates the high dependency of the method to the quality of the baseline model. For the sequential scheme model and data fit is also slightly improved, but it still presents lots of large scale and high amplitude artefacts. Concerning the double difference scheme, results with the smoothed 1-D model is close to the one obtained with the baseline model and presents similar data fit. Two additional tests are performed for double difference inversions using respectively the exact 1-D true model and an homogeneous model as starting models. The four double difference models tested all recover the time-lapse anomalies at their right positions and result in images with very few artefacts. However, it is clear that the magnitude and resolution of the time-lapse variations are related

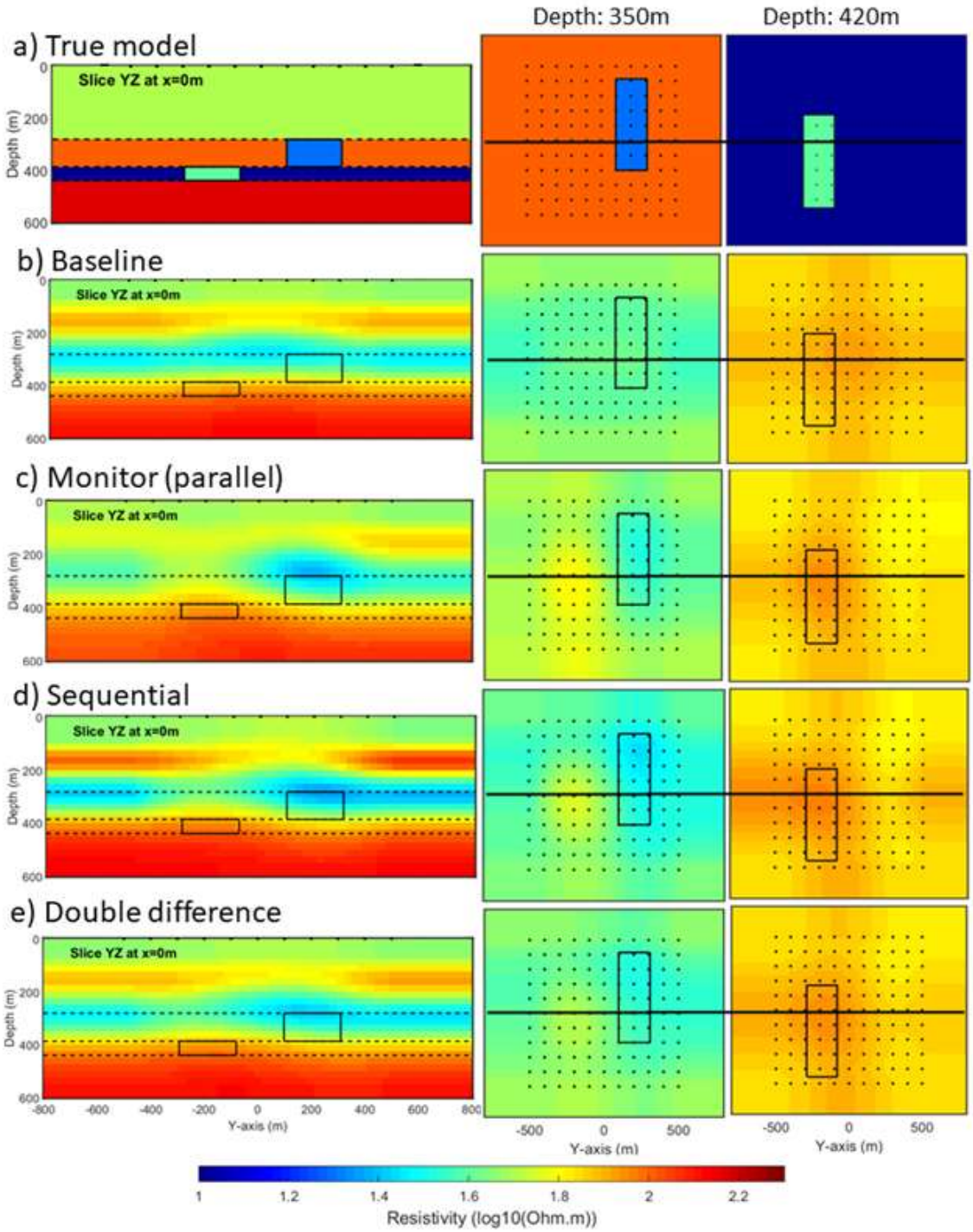

Figure 2. Slices of 3-D resistivity models: (a) exact model, (b) baseline model, (c) monitor model from parallel inversion, (d) monitor model from sequential inversion, (e) monitor model from double difference inversion. First column are slices along the YZ directions (in-depth) and the two last columns are slices at specific depths (350 m and 420 m). All inversions have a homogeneous starting model at 50 $\Omega.m$. Dashed lines on depth slices indicate interfaces of the true model (a). Black rectangles highlight regions of the model changing between time-steps in the true model. Thick black lines on constant depth plots are positions of the associated depth slice.

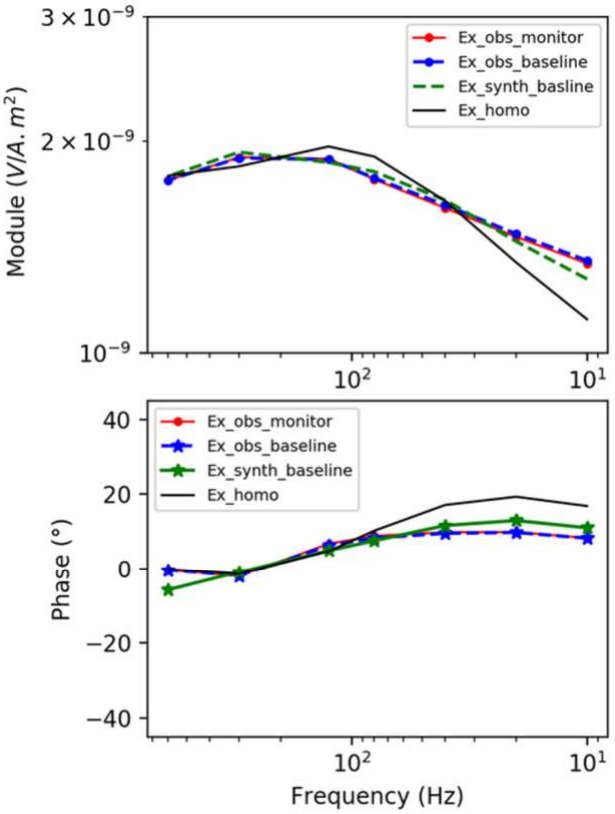

Figure 3. Data spectrum for the dominant component of a central station - Modulus and phase. Black line : $50\,\Omega.m$ homogeneous background. Red line: "observed" monitor data. Dashed blue line: "observed" baseline data. Green line: data computed in the baseline inversion model of figure 2b.

to the quality of the baseline model which is used. With the exact model (Figure 7e), the amplitude variations of the conductive anomaly are close to the true variations and the time-lapse is very well fitted with a RMS of 0.24% close to the level of the forward modeling accuracy. An interesting point is that even using a homogeneous model very far from the baseline model, the anomalies are very well imaged, at their right position (Figure 7f). The amplitude of the anomalies are however much weaker in this case and the double difference data fit is much lower (RMS = 1.72%).

4.3 Robustness with noise

Time-lapse signals may be small compared to inversion strategies biases, but it can also be small compared with noise level. It is therefore necessary to investigate the behavior of the three time-lapse inversion approaches in the presence of noise. We can consider two kind of noise on EM measurements. The first is a random noise proportional to the amplitude of the recorded field. The second is a bias or a data shift typical of CSEM or MT surveys. Generally, the static shift effect (galvanic distortion) is due to unresolvable shallow anomalies or data processing bias. In order to simulate challenging

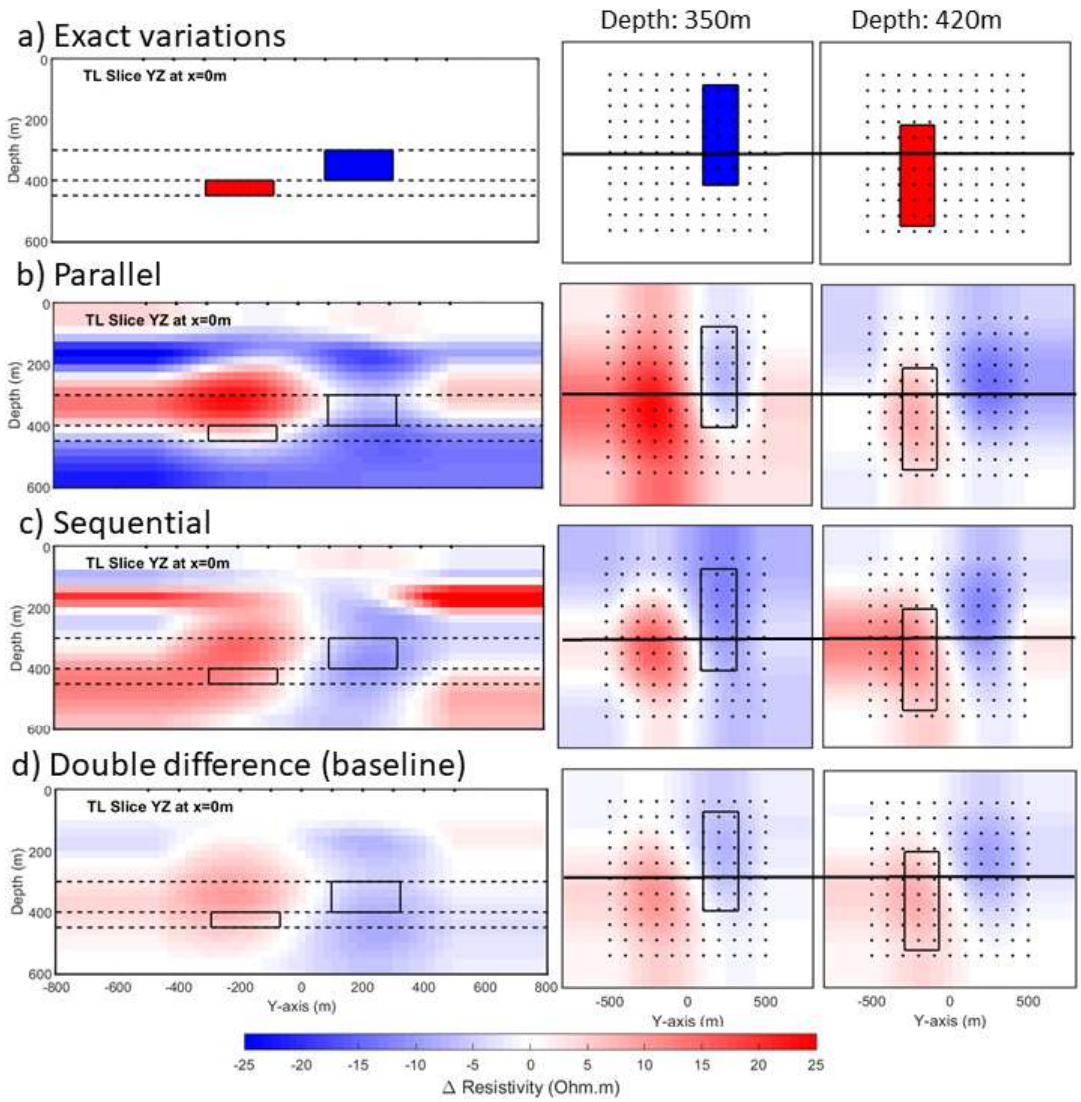

Figure 4. Slices of 3-D time-lapse resistivity variations: (a) exact time-lapse targets, (b) parallel difference model, (c) sequential difference model, (d) double difference model, using baseline reconstructed from an homogeneous model. First column are slices along the YZ directions (in-depth) and the two last columns are slices at specific depths (350 m and 420 m). Dashed lines on depth slices indicate interfaces of the true model. Black rectangles highlight regions of the model changing between time-steps in the true model. Thick black lines on constant depth plots are positions of the associated depth slice.

noisy monitoring data, we added this two kinds of noise to the previous baseline and monitor data. We firstly select randomly 10 of the 121 stations and apply a factor 2 on all the fields recorded at these position (E_x/E_y for all sources and all frequencies) to simulate a significant static shift. Then we add to all the stations a 1% of random Gaussian noise proportional to the modulus and phase, respectively. Noise are then propagated accordingly to real and imaginary parts of the electric fields, which are the

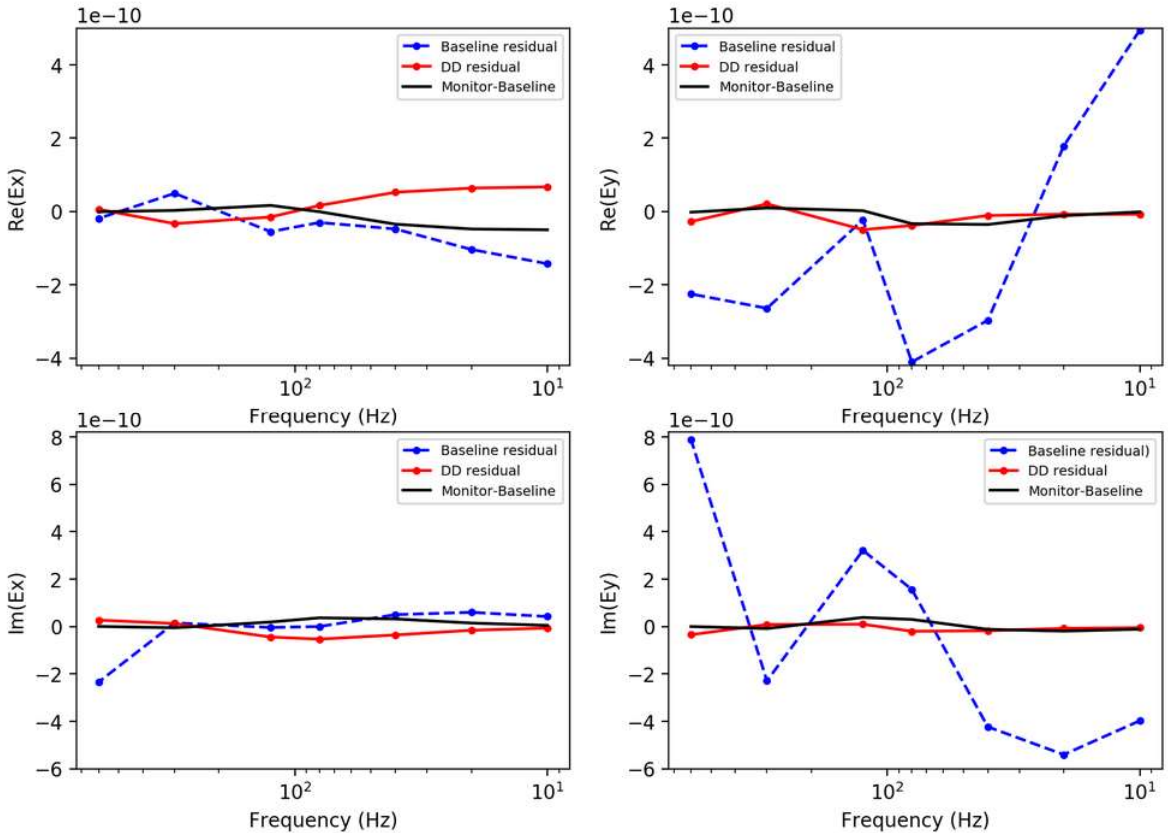

Figure 5. Weighted data residuals (real and imaginary parts of both electric field components) for a central station. Black line: initial double difference data $(d_{obs2} - d_{obs1})$, Red line: double difference (DD) data residuals after inversion, Blue dashes: data residuals of the baseline after inversion.

inverted variables. Noise levels are chosen to be at the same level than CSEM repeatability (Darnet et al. 2018; Tietze et al. 2019).

A new inverse data covariance vector $\mathbf{W_d}$ is built based on the new data set. The baseline and monitor data are then inverted separately following parallel inversion strategy. Those inversions result in poorly reconstructed resistivity models (figure 8a-c) with poor data fit (RMS 15%). The 1-D structure of the baseline is roughly imaged but the models include artefacts and the resistivity contrasts are more underestimated than without noise. The high final RMS is explained in particular by outliers in the data caused by the static shifts that inversion cannot explain with the given coarse parameterization. The model difference figure 8b shows that parallel difference can recover both anomalies similarly as with the clean data and with a similar resolution but with less pronounced contrasts. The sequential difference inversion however completely fails to converge. Sequential difference is affected by the part of the data which remains unexplained in the baseline. As the RMS is high in the presence of high level of noise, sequential difference is particularly affected. The double difference inversion

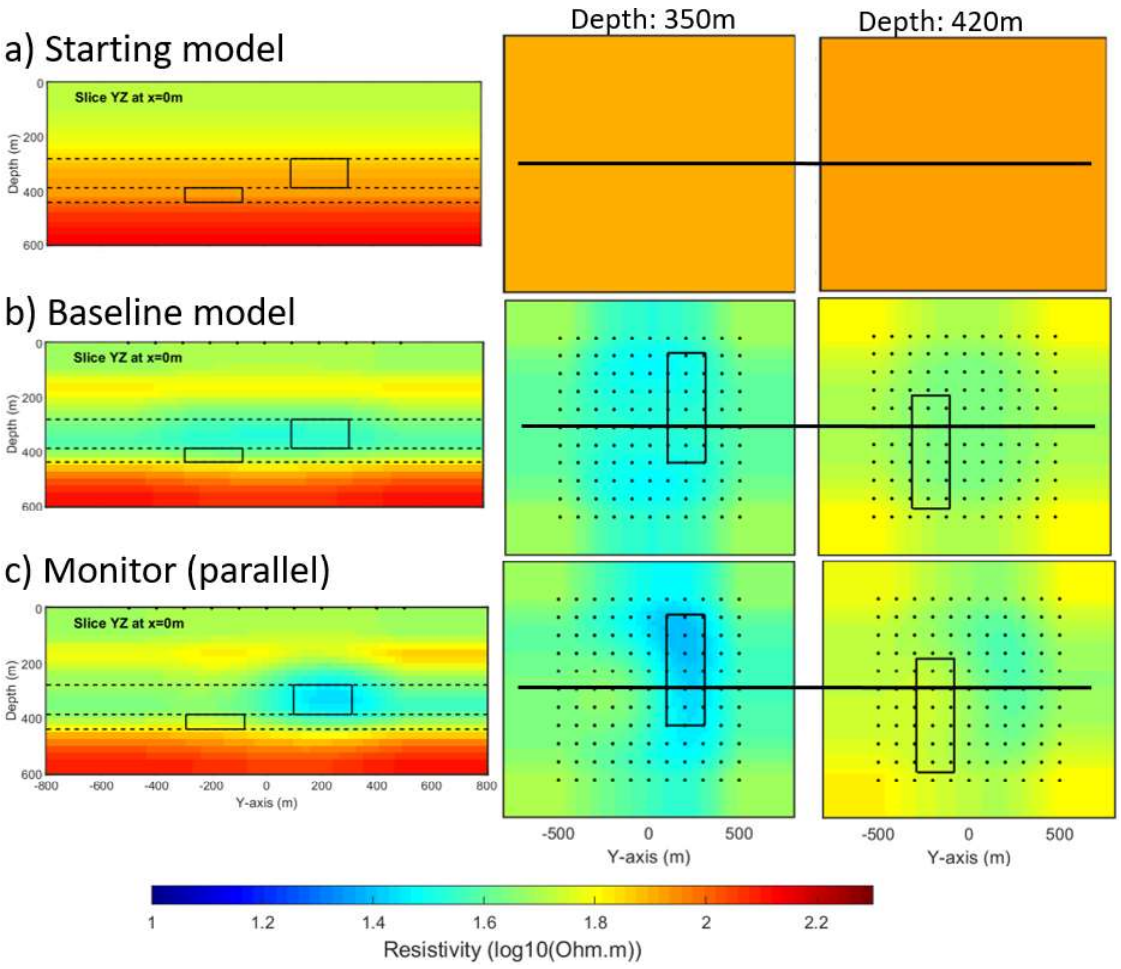

Figure 6. Slices of 3-D resistivity models: (a) smooth starting model, (b) baseline model, (c) monitor model from parallel inversion. A smooth 1-D model is used as starting model. First column are slices along the YZ directions (in-depth) and the two last columns are slices at specific depths (350 m and 420 m). Black rectangles highlight regions of the model changing between time-steps in the true model. Thick black lines on constant depth plots are positions of the associated depth slice.

is however not affected by the static shift which is similar for the two data set. This implies a weak dependence to the baseline model quality for the double difference scheme. The double difference model (figure 8c) shows both anomalies at their right positions with very few artefacts and significant RMS reduction (RMS 2.89% to 2.28%).

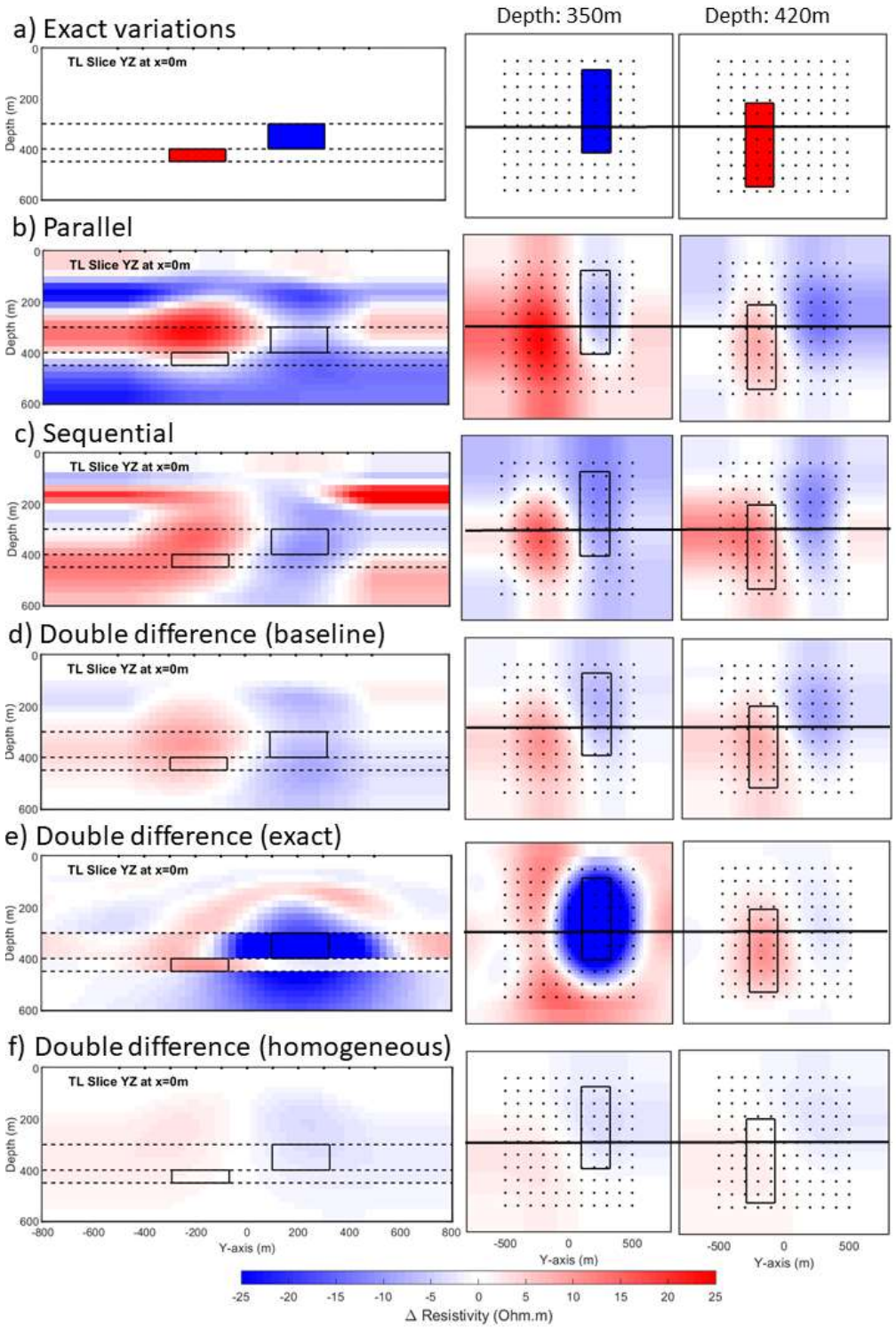

Figure 7. Slices of 3-D time-lapse resistivity models: (a) targets, (b) parallel, (c) sequential, (d) double difference, using a baseline reconstructed from the smooth 1D model, (e) double difference model using the exact baseline as a starting model and (f) double difference model using an homogeneous background as a starting model. First column are slices along the YZ directions (in-depth) and the two last columns are slices at specific depths (350 m and 420 m). Dashed lines on depth slices indicate interfaces of the true model. Black rectangles highlight regions of the model changing between time-steps in the true model. Thick black lines on constant depth plots are positions of the associated depth slice.

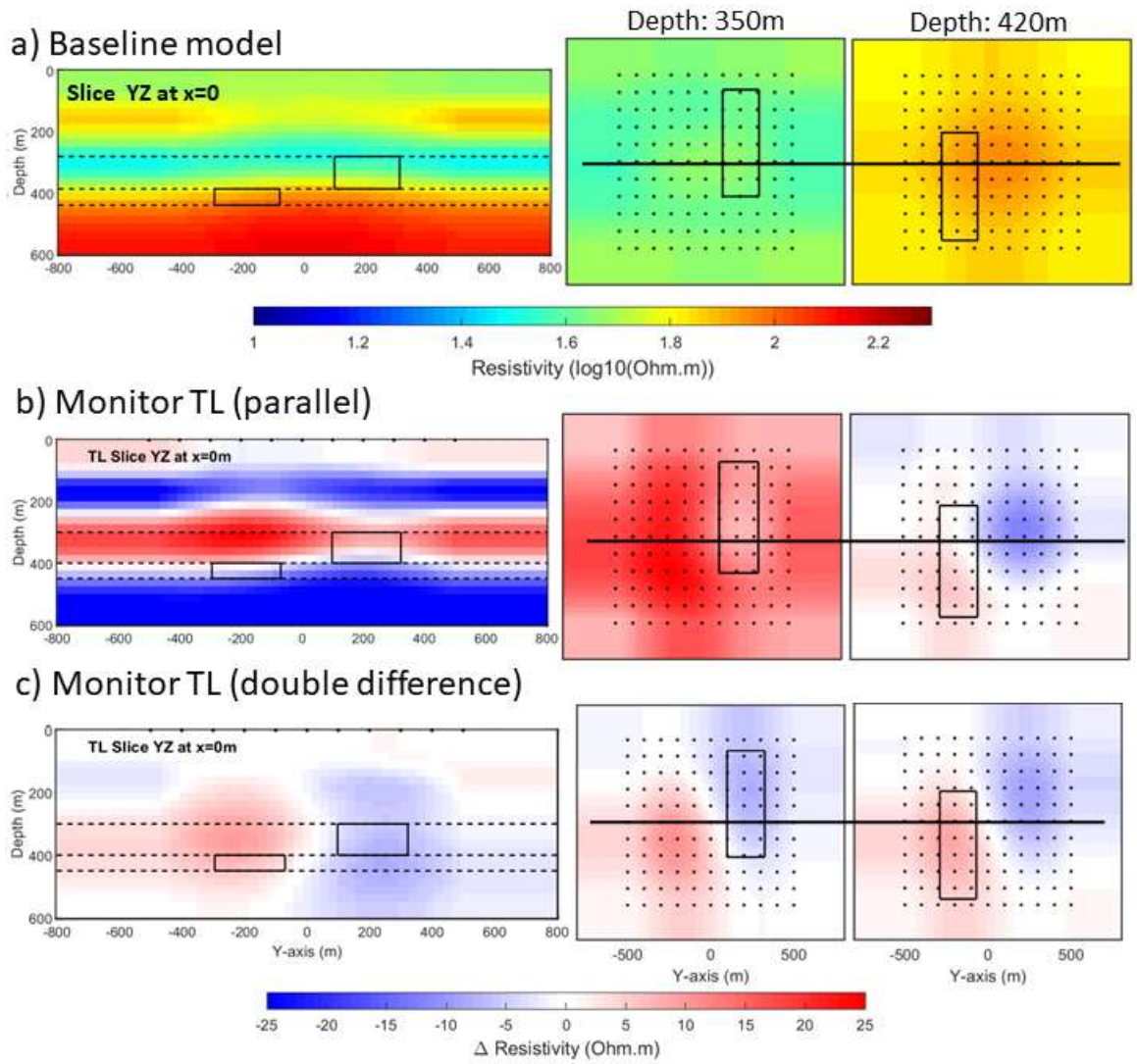

Figure 8. 3-D resistivity and time-lapses (TL) models reconstructed from noisy data: (a) baseline model reconstructed starting from an homogeneous background, (b) parallel TL, (c) double difference TL. First column are slices along the YZ directions (in-depth) and the two last columns are slices along a specific depths (350 m and 420 m). Dashed lines on depth slices indicate interfaces of the true model. Black rectangles highlight regions of the model changing between time-steps in the true model. Thick black lines on constant depth plots are positions of the associated depth slice.

5 APPLICATION TO THE REYKJANES GEOTHERMAL FIELD

5.1 CSEM survey on Reykjanes Geothermal Field

The Reykjanes geothermal field is located at the south-west of Iceland at the landward extension of the Reykjanes Ridge (figure 9, Darnet et al. (2018)). The geothermal reservoir is located below 4 km depth and was stimulated to improve the efficiency of the well. However, CSEM penetration depth

is generally below 2.5 km which is not suitable to monitor such deep changes. Nevertheless, before the production start in 2006, the geothermal fluid was mainly liquid. According to Gudmundsdottir (2015), the geothermal production would induce a pressure drop inside the reservoir and would cause a steam cap development at depth above 1100 m. These depths can be investigated by CSEM but the increase of resistivity induced by the steam cap development is unknown. We would like to know if such changes are detectable and could be monitored with CSEM techniques. Two surveys are acquired one year apart, a first one in September 2016, while drilling of RN-15/IDDP-2 well. The other is performed in August 2017, after the thermal stimulation of the RN-15/IDDP-2 well. Two orthogonal horizontal electric dipoles are used as sources (figure 9), 3 km north of the geothermal field. They provide two polarizations called POL1 (744m-long dipole between E1 and E2) and POL2 (670m-long dipole between E2 and E3). Receivers record the three orthogonal component of the magnetic field and the two orthogonal components of the horizontal electric field. Specific care have been taken for setting sources and receivers at the exact same location between baseline and monitor surveys. Precise locations are determined with differential GPS (d-GPS) allowing a centimeter precision on locations. A complete description of the survey can be found in Darnet et al. (2018).

5.2 CSEM data quality: time-lapse feasibility analysis

Darnet et al. (2018) assess the influence of internal and external noise on survey repeatability between the two acquisitions. Over the whole frequency band, repeatability is within 2-3% and 2-3° for the amplitudes and phases respectively. On specific frequency bands, the presence of strong external noise degrades significantly the repeatability up to 10% and 10° on the amplitudes and phases, respectively (e.g., 32 s at low frequencies, 50 Hz and harmonics at high frequencies).

In order to identify time-lapse signals related to thermal stimulation of the reservoir through the RN-15/IDDP2 well, Darnet et al. (2018) analyze the amplitude and phase changes of the polarization ellipse for the horizontal electric field between the monitor and baseline surveys. Detailed analysis for each station signal shows no clear and consistent time-lapse anomaly related to the RN-15/IDDP-2 thermal stimulation. However, the stimulated zone is deep (> 4 km) and the CSEM sensitivity for time-lapse signal is weak a this depth. Since CSEM technique is a diffusive method, weak signals may appear by exploiting the spatial coherence of variations amongst all station and not only individually. For this reason, we aim at using 3-D time-lapse differential inversion to map those weak potential variations at their right positions.

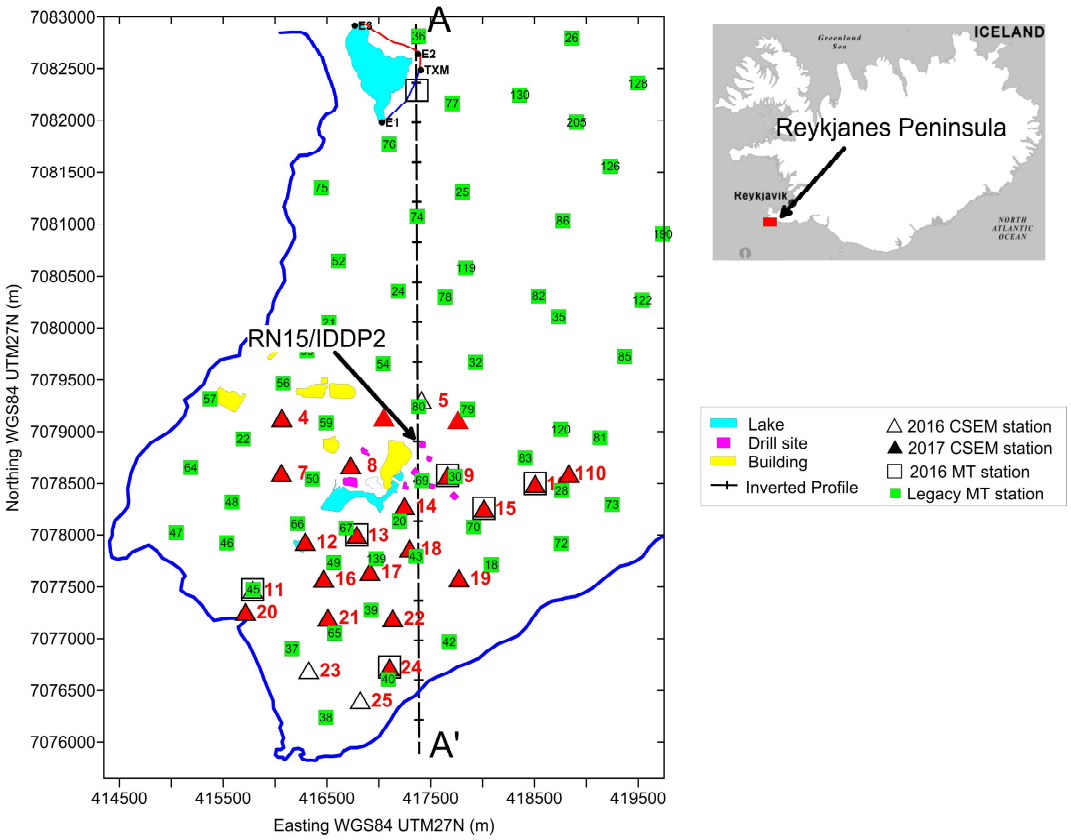

Figure 9. Map of the Reykjanes geothermal field and time-lapse CSEM and MT survey layout. CSEM transmitter is labelled TXM with the two different polarizations E1-E2 and E2-E3. Recording stations are symbolized by red triangles with numbers. Section AA' represents the direction of 2-D slices from the inverted 3-D model intersecting the RN15/IDDP2 well.

5.3 Baseline inversion

We extract common receiver/component data between baseline and monitor surveys, which is a requirement for the double-difference strategy. To avoid poorly repeatable data due to noise contamination, we remove low (> 32 s) and high frequency data (> 10 Hz). Real and imaginary parts of the horizontal electric field are inverted for 9 frequencies [0.09125, 0.125,0.375,0.5,0.625,0.875,1,2,8] Hz.

From the first data set, we build the baseline model noted m_1 by using a steepest-descent gradient optimization algorithm available in POLYEM3D. The starting model is homogeneous with a resistivity set at 20 Ω.m. The inversion is stopped after 200 iterations with an horizontal smoothing window of 500 m to remove the sensibility to singularities at station positions. An additional preconditioning is used to limit too high sensitivity close to the transmitters and compensate for loss of sensitivity with depth (Plessix & Mulder 2008).

Baseline reconstruction depicts the resistivity variations from the data set acquired in September

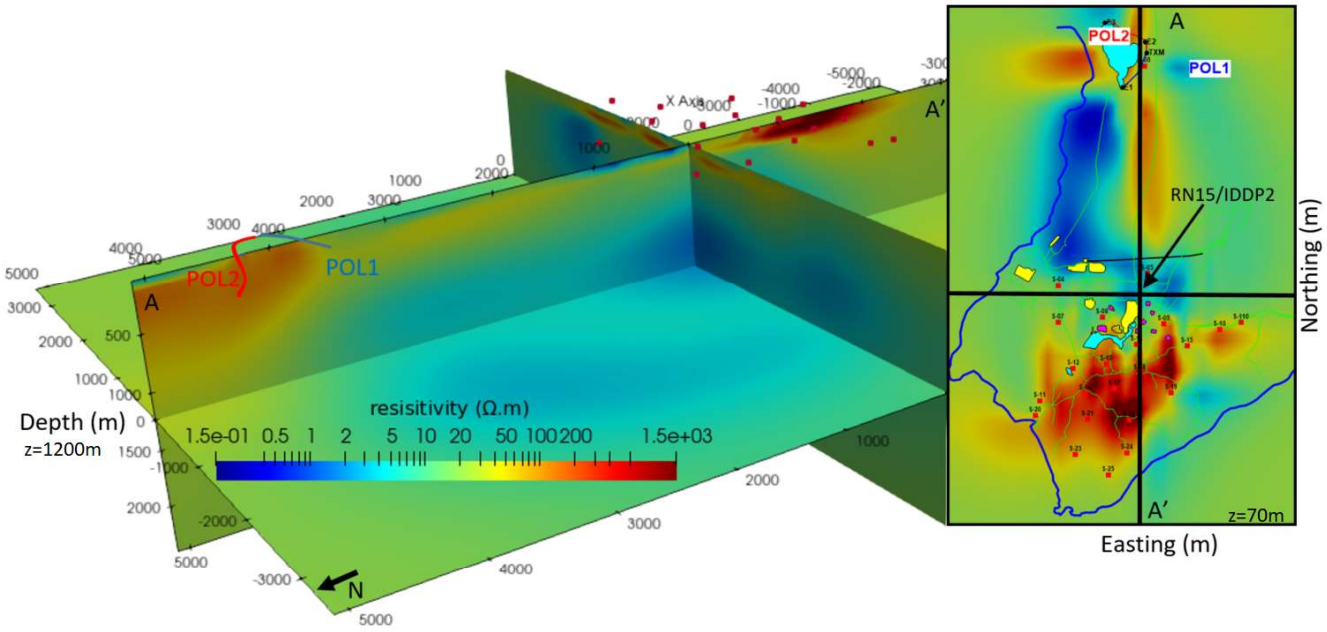

Figure 10. 3-D view of the baseline model. Red dots indicate the receiver locations and blue dots the extremities of the source cables for POL1 and POL2. The RN15/IDDP2 well is located at the intersection of the two vertical slices. With the vertical N-S section is indicated on figure 9. The horizontal slice is displayed for a depth of 1200 m depth. Bottom right inset is the horizontal slice at surface. Roads are represented by thin green lines.

2016 (Figure 10). The baseline inversion underlines a highly resistive shallow layer down to 250-300 m depth with a thickening toward the South. Deeper, a bubble-shape zone located at 1.2 km depth at the center of the model is characterized by low resistivities (1-2 Ω.m). At the surface, a low resistivity region seems to follow the coastline in the northern part of our survey. This anomaly must be related to the sea or seawater intrusion inland (Georgsson 1981). Although our inversion are affected by the ocean we decided to not model its effects, it is limited by several aspects. First, since ocean is not directly present between the source and receivers the effect will be limited. But with or without ocean layer in the modeling we retrieve a very conductive anomaly in the model between the source and the receivers. This is mainly due to strong saline water infiltration in-land reported by previous studies (large ERT profiles, Georgsson (1981)). Thus, including (or not) water in the modeling is not giving very different results for the baseline. Second, from a time-lapse point of view this effect will be considered as static shift and will be removed using the double difference strategy. As a consequence, main results will not be changed by including or not the water in the modeling.

To assess the quality of the inversion, data misfit between observed and predicted data is analyzed as shown for stations 8, 14 and 18 in figures 11, 12 and 13. Module and phase are compared for predicted data at the last and first iteration with the observed data. We see a good improvement both in module and phase over the studied frequency band. The starting RMS is 125% and ends up at 28%

at the last iteration. Black lines (prediction for an homogeneous medium) are quite far of the observed data for the y-component compared to the x-component. A substantial improvement appeared for the y-component in phase and module for data predicted at the end of the inversion process. A change of sign of the electric field is observed around 0.7Hz, with significant variations of the phase at this frequency.

To cross-validate the resistivity model, we superimpose at the RN15 well location a resistivity log (Figure 14 a). This reinterpreted log is defined from the observed resistivity log of the RN15/IDDP2 well (Reinsch 2016) and surface geology (no data shallower than 200 m). On field, the shallowest layer is composed of relatively unaltered recent lava flows fitting well with the high resistivity in surface in the south part. A strong resistivity change can be seen between the North and the South part (see horizontal slice of figure 10). We can notice a low-resistivity structure around the RN15/IDDP2 well located at the intersection of the two vertical slices (Figure 10). Below the lava layer, the resistivity log indicates a more conductive layer (1 Ω.m) over 800 m overlaying a 20 Ω.m on 1150 m. The conductive layer is considered as the cap of the geothermal reservoir. Due to the limited penetration depth of CSEM method and local geology we cannot reasonably sound deeper than 2 km.

5.4 Parallel, sequential and double-difference on the Reykjanes site

Once an acceptable baseline is found, we proceed to the inversion of the monitor data. First, we test the double difference scheme which gives the best results for synthetics with noise. The main structures are recovered between the baseline and the monitor inversion (Figure 14 (b,c)). For instance, the clear thickening of the shallow resistive layer toward the South is clearly visible on both sections (between 4200 to 5200 m along the section on figure 14 (b,c)). For the double difference strategy, RMS is equal to 1% and reaches a minimum at 0.6% after 200 iterations. Comparisons between baseline and monitor model are not straightforward since we expect a small time-lapse signal. To do so, absolute and relative differences are computed between the baseline and monitor models.

Absolute differences highlight the highest resistivity variations whereas relative changes emphasize on larger variations according to the baseline values. Because of the presence of high resistivity lava, we expect larger absolute variations in the first hundred meters. As a matter of fact, larger time-lapse signals occur over the first 500 m below the surface. A relative change of -4.8 % can be observed for the first hundred meters between 4200 to 6000 m away from the source. If such variations are resolved and not dominated by noise propagation, it may be induced by water content variations inside basalt layer that might have changed between the two surveys. Nonetheless, relative difference from the baseline model show deeper variations down to 1200 m but at lower values. Deeper 500 m, relative variations goes below 3 % which implies a time-lapse signal at the threshold of repeatability.

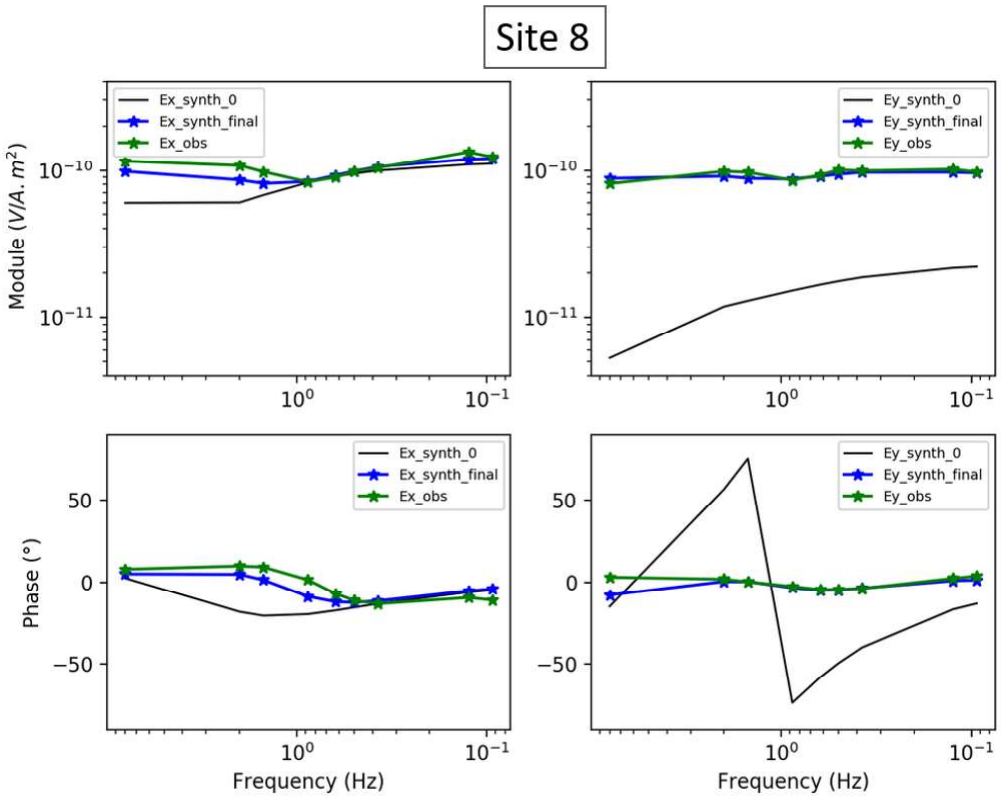

Figure 11. Module and phase of the horizontal electric field. The electric field is represented along the x-component (left column) and y-component (right column). Predicted data for an homogeneous model at 20 Ω.m (black lines), observed data (blue lines with stars) and synthetics at the 200th iteration of the 3-D inversion (green lines with stars) are displayed. Station location can be found on figure 9.

The time-lapse model is dominated by an increase of resistivity with a noticeable negative time-lapse signal between 500-1000 m depth below the RN15 well. But such changes indicate time-lapse changes of the same order than repeatability level (2-3%) except for subsurface variations (-4.8% at 4400 m and 6.28% 3700 m away from the source for a depth of 200 m). Such changes suggest no temporal changes of the resistivity or below the detectability threshold for the studied frequencies ($< 2 - 3\%$).

To assess performances of the different time-lapse inversion strategies, we apply the three previous schemes to the real data set of Reykjanes. Parallel, sequential and double difference inversion schemes are conducted. Figure 14 shows the absolute and relative differences for the three schemes: (d,e) double difference, (f,g) sequential and (h,i) parallel schemes. The relative difference for the sequential inversion indicates large negative decrease of resistivity at depth of 1100 m with a value of 4.9%. Unlike the relative difference of the double difference scheme, higher values are no more located at the shallower layer of the model but at depth of 1000 m. These differences might be induced by a combinations of several factors. Temporal changes may have an impact on relative differences, but

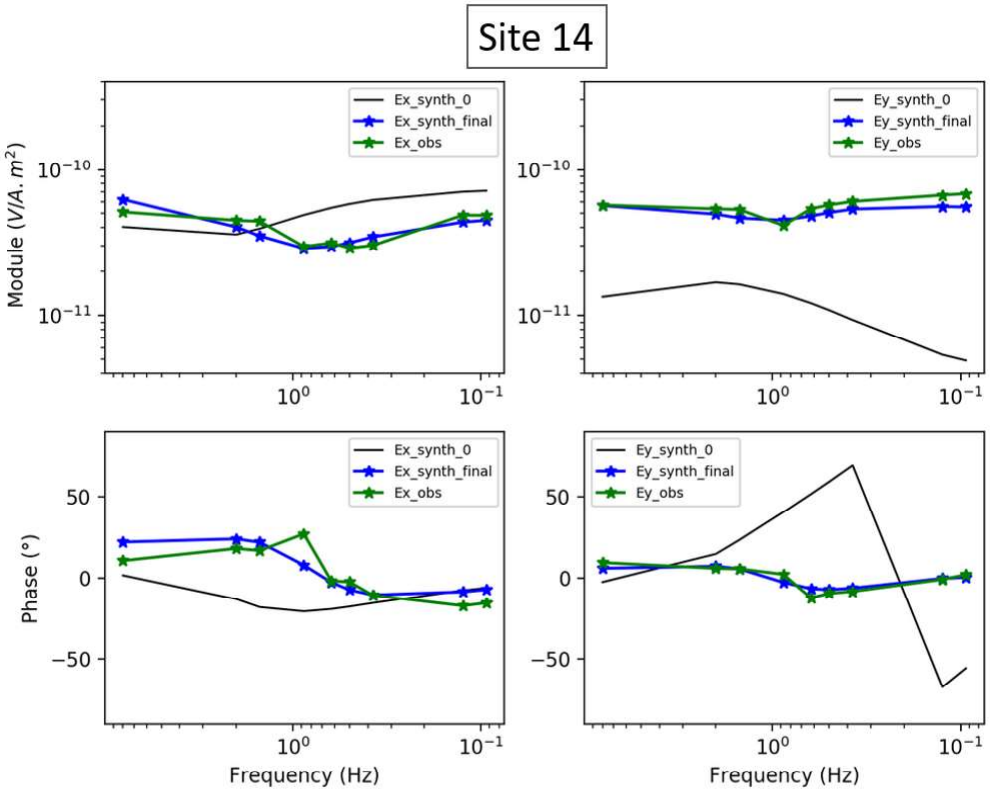

Figure 12. Module and phase of the horizontal electric field. The electric field is represented along the x-component (left column) and y-component (right column). Predicted data for an homogeneous model at 20 Ω.m (black lines), observed data (blue lines with stars) and synthetics at the 200th iteration of the 3-D inversion (green lines with stars) are displayed. Station location can be found on figure 9.

signals from the unfitted data of the baseline inversion can be mapped in the time-lapse model. If the baseline model is properly recovered, time-lapse signal for the sequential inversion should be close to the double difference inversion. In this case, baseline reconstruction seems to be insufficient for proper use of the sequential scheme.

Relative changes for the parallel inversion look closer of the double difference with noticeable differences in the amplitudes (Figure 14 (h,i)). Strong amplitudes are visible at 1100 m with positive anomaly above 8% which is well above the detectability threshold. High amplitudes can be mainly attributed to the strong non-uniqueness in CSEM problems. In that case, we may easily conclude to an increase of resistivity at depth of 1100 m where such changes are expected from the steam cap development.

Though, we should remind the plurality of factors polluting the time-lapse signals. For parallel inversions: unfitted baseline structures, static shift structures and noise (correlated and not) are inverted in the same time as temporal resistivity changes. So far, we have no tool to discriminate between these

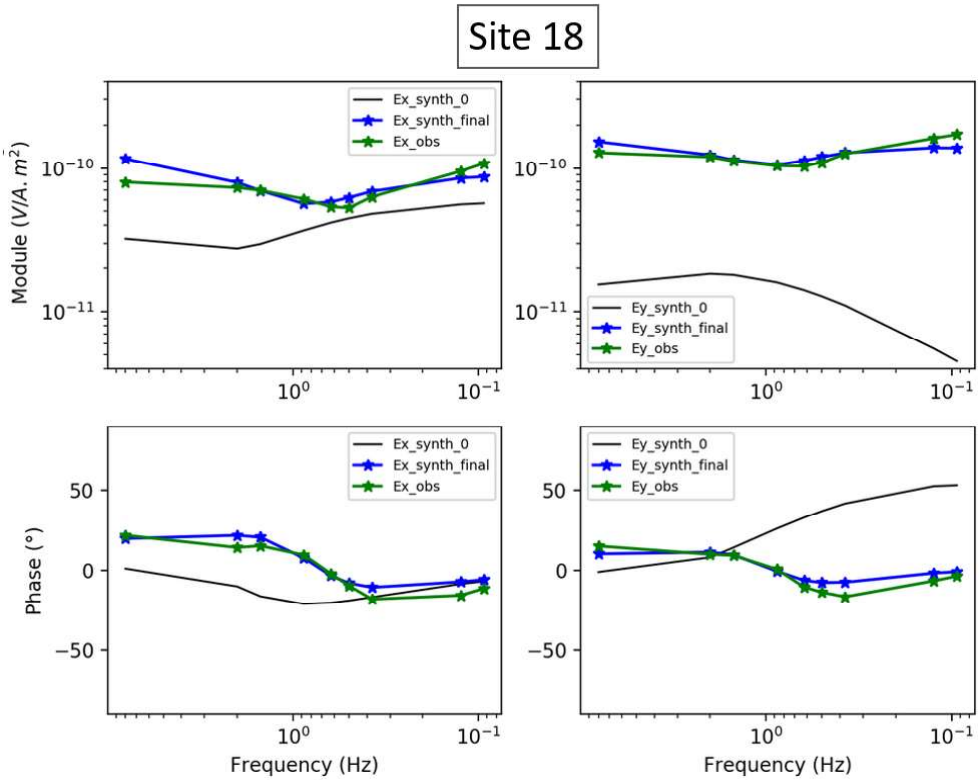

Figure 13. Module and phase of the horizontal electric field. The electric field is represented along the x-component (left column) and y-component (right column). Predicted data for an homogeneous model at 20 Ω.m (black lines), observed data (blue lines with stars) and synthetics at the 200th iteration of the 3-D inversion (green lines with stars) are displayed. Station location can be found on figure 9.

different factors through the parallel inversion. The resistivity increase could be a time-lapse signal from the steam cap as well as the focusing of data noise.

6 DISCUSSIONS AND CONCLUSIONS

In this study we investigate several time-lapse inversion strategies to infer the temporal changes of resistivity. We compare the commonly used parallel inversion framework with the sequential and double difference schemes. The dependence of the three techniques to the starting model is studied, and we assess their robustness to noise. Parallel difference is the most straightforward and commonly used approach in resistivity monitoring. Since the inverse problem is non linear, this approach is dependant on the inversion path, and therefore on the starting model. In case where the starting model is rough and far from the solutions, the paths are very different between baseline and monitor inversion, and the model difference may results in artefacts including large scale structures only due to the different inversion paths. This approach is also sensitive to correlated and uncorrelated noise.

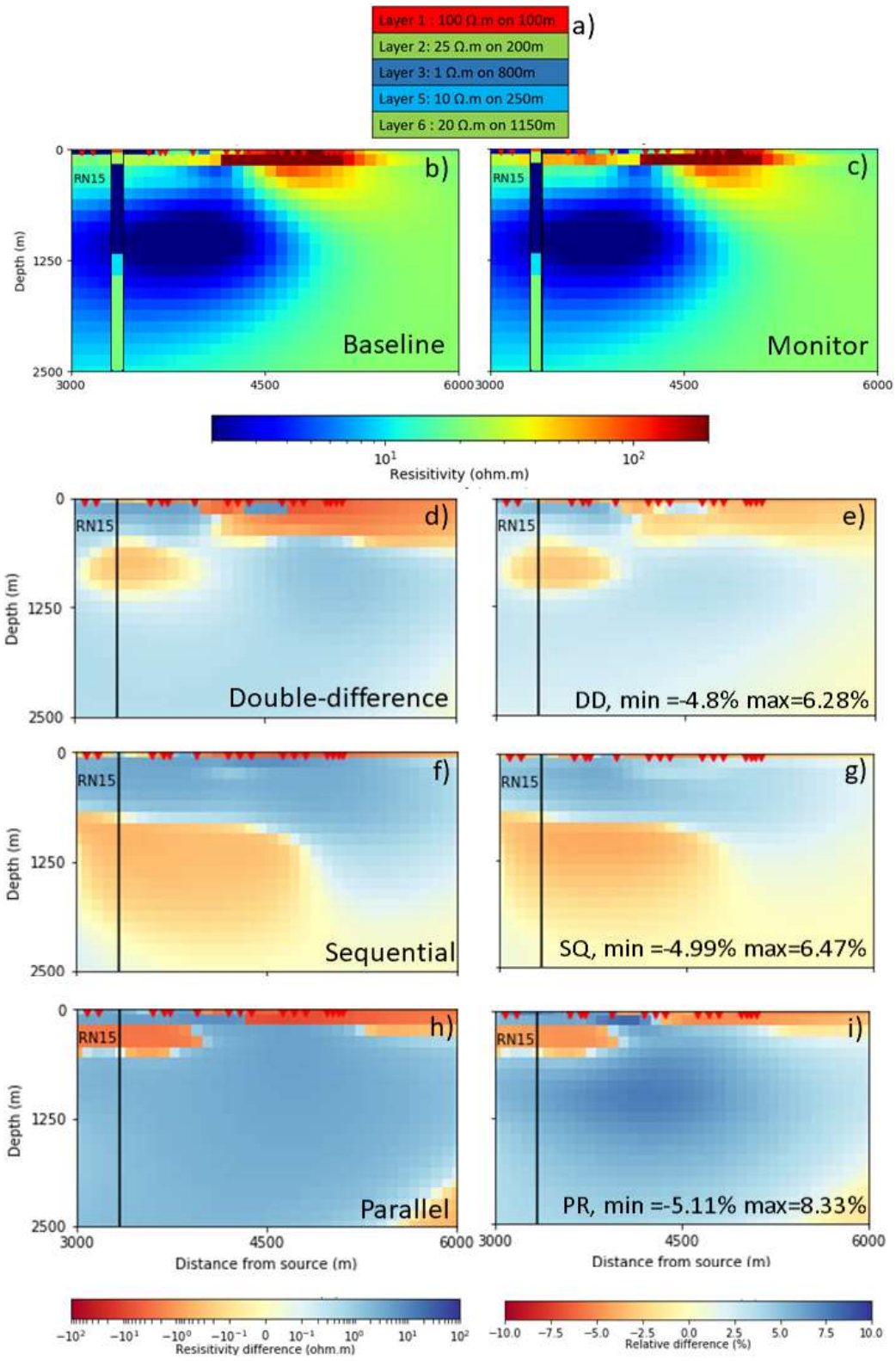

Figure 14. a) Interpreted resistivity log at the RN15/IDDP2. North-South sections of (b) the baseline inversion with a starting model at 20 Ω.m, (c) monitor inversion using the double difference scheme with baseline model as starting model. Time-lapse sections computed with (d,e) double difference (DD) (f,g) sequential (SQ) (h,i) parallel (PR) inversion scheme. (Left column) simple difference between monitor and baseline (right column) relative difference compared to the baseline. Well RN15/IDDP12 is displayed as a vertical black lines on cross-sections. Reversed red triangles are the projected locations on the cross-sections of all CSEM receivers used in the inversion.

Sequential inversion scheme starts with the baseline model construction. We show on synthetics that this approach is very dependant on the quality of the baseline model and can easily produces in the monitor model artefacts caused by unexplained parts from the baseline inversion. Therefore, this approach is highly dependant on the starting model and on the static noise which strongly affect the data fit of baseline inversion.
On the other hand, the double difference inversion (or differential inversion) focuses on the time-lapse signal only. By isolating the time-lapse signal it allows to focus exclusively on temporal resistivity changes. We show this approach is much more robust to noise because static noise and modelling errors are completely removed. Double difference is also less dependant on the starting model. In particular, we demonstrated on synthetic experiments that even starting from an very rough initial model such as an homogeneous resistivity background, the double-difference inversion maps the resistivity anomalies to their right place and generates very few artefacts. Quantitative estimation of the time-lapse resistivity variations however is still dependant on the quality of the baseline model. It is also interesting to note that using double-difference inversion allows to fit time-lapse signals that are lower to baseline inversion data residual level, and also lower that total signal noise level. It is also possible to image and localize resistivity variations even without a proper baseline reconstruction, or with a baseline model built with independent information. For instance, a large scale baseline model could be built with well logs, geological knowledge or a dense EM geophysical survey, and the monitoring performed with a reduced subset of the EM survey kept permanent between time steps.

These comparisons are applied to a time-lapse land CSEM survey acquired at 1-year of interval over the Reykjanes geothermal field before and after a stimulation phase. A potential time-lapse signal generated by the steam cap development is expected to be small and we should not see important variations during the time. The double-difference strategy highlights no peculiar signals coming from the geothermal exploitation with relative difference below the repeatability threshold. Sequential and parallel schemes would suggest significant but inconsistent temporal changes in the resistivity of the medium considering the repeatability rate. But as shown with synthetic tests, these time-lapse signals are contaminated by potential incomplete reconstruction of the baseline and by the strong non-linearity of the inversion process.

A next step would be to quantify the ratio between time-lapse signal and the combination of the uncorrelated noise for the double difference scheme. Of course, random noise is never reduced by data combination and it would be interesting to analyze the impact of the noise propagation on the time-lapse resistivity changes. Since the CSEM problem is intrinsically non linear noise propagation study is not straightforward and Bayesian recipes would maybe be useful to look over that point. An

other point that was not explored in this paper is the high potential of combining prior information, and in particular geometrical constrains often available in time-lapse studies, to the time-lapse differential imaging. Nevertheless, double-difference strategy is a remarkable tool for geophysical monitoring and especially for strongly non-linear problems such as resistivity imaging, which has to be preferred over the other inversion schemes when it is possible. Its use may certainly improve the current inversion philosophy for time-lapse problem in resistivity monitoring.

ACKNOWLEDGMENTS

The research and developments of the POLYEM3D code leading to these results has received fundings from the French ANR project EXCITING. Acquisition and processing of the Reykjanes dataset has been funded by the European research program H2020 in the framework of the project DeepEGS N°690771. Large scale 3D EM modeling and inversion was performed with BRGM's POLYEM3D code on the Occigen supercomputer thanks to GENCI (Grand Equipement de Calcul Intensif) and CINES (Centre Informatique National de l$'$enseignement Supérieur) super computing facilities. We would like to thank Florent Beaubois and Mariane Peter for their help during the CSEM acquisition.

DATA AVAILABILITY

The data underlying this article will be shared on reasonable request to the corresponding author.

REFERENCES

Abdelfettah, Y., Sailhac, P., Larnier, H., Matthey, P.-D., & Schill, E., 2018. Continuous and time-lapse magnetotelluric monitoring of low volume injection at Rittershoffen geothermal project, northern Alsace–France, *Geothermics*, **71**, 1–11.

Ajo-Franklin, J. B., Minsley, B. J., & Daley, T. M., 2007. Applying compactness constraints to differential traveltime tomography, *Geophysics*, **72**(4), R67–R75.

Amestoy, P., Duff, I. S., Koster, J., & L'Excellent, J.-Y., 2001. A Fully Asynchronous Multifrontal Solver Using Distributed Dynamic Scheduling, *SIAM Journal on Matrix Analysis and Applications*, **23**(1), 15–41.

Amestoy, P., Buttari, A., L'Excellent, J.-Y., & Mary, T., 2019. Performance and Scalability of the Block Low-Rank Multifrontal Factorization on Multicore Architectures, *ACM Transactions on Mathematical Software*, **45**, 2:1–2:26.

Asnaashari, A., Brossier, R., Garambois, S., Audebert, F., Thore, P., & Virieux, J., 2014. Time-lapse seismic imaging using regularized full-waveform inversion with a prior model: which strategy?, *Geophysical prospecting*, **63**(1), 78–98.

Bretaudeau, F., Coppo, N., Wawrzyniak, P., Penz, S., & Girard, J.-F., 2016. A pseudo-MT formulation for 3D CSEM inversion with a single transmiter.

Commer, M. & Newman, G. A., 2008. New advances in three-dimensional controlled-source electromagnetic inversion, *Geophysical Journal International*, **172**(2), 513–535.

Darnet, M., Wawrzyniak, P., Coppo, N., Nielsson, S., Schill, E., & Fridleifsson, G., 2018. Monitoring geothermal reservoir developments with the Controlled-Source Electro-Magnetic method—A calibration study on the Reykjanes geothermal field, *Journal of Volcanology and Geothermal Research*.

De Donno, G. & Cardarelli, E., 2017. VEMI: a flexible interface for 3D tomographic inversion of time-and frequency-domain electrical data in EIDORS, *Near Surface Geophysics*, **15**(1), 43–58.

Georgsson, L. S., 1981. Resistivity survey on the plate boundaries in the western Reykjanes Peninsula, Iceland, *Trans.-Geotherm. Resour. Counc.;(United States)*, **5**(CONF-811015-).

Grayver, A. V., Streich, R., & Ritter, O., 2013. Three-dimensional parallel distributed inversion of CSEM data using a direct forward solver, *Geophysical Journal International*, **193**(3), 1432–1446.

Gudmundsdottir, V., 2015. Svartsengi – Reykjanes: Reservoir Temperature and Pressure Monitoring Report 2014, *Iceland GeoSurvey report*, **ISOR-2015/026**.

Gupta, A., Joshi, M., & Kumar, V., 2001. WSMP: A high-performance serial and parallel sparse linear solver.

Houser, C., Masters, G., Shearer, P., & Laske, G., 2008. Shear and compressional velocity models of the mantle from cluster analysis of long-period waveforms, *Geophysical Journal International*, **174**(1), 195–212.

Karaoulis, M., Revil, A., Werkema, D., Minsley, B., Woodruff, W., & Kemna, A., 2011. Time-lapse three-dimensional inversion of complex conductivity data using an active time constrained (ATC) approach, *Geophysical Journal International*, **187**(1), 237–251.

Kuo, B.-Y., Forsyth, D. W., & Wysession, M., 1987. Lateral heterogeneity and azimuthal anisotropy in the North Atlantic determined from ss-s differential travel times, *Journal of Geophysical Research: Solid Earth*,

92(B7), 6421–6436.

Métivier, L. & Brossier, R., 2016. The SEISCOPE optimization toolbox: A large-scale nonlinear optimization library based on reverse communication: The SEISCOPE optimization toolbox, *Geophysics*, **81**(2), F1–F15.

Miller, C. R., Routh, P. S., Brosten, T. R., & McNamara, J. P., 2008. Application of time-lapse ERT imaging to watershed characterization, *Geophysics*, **73**(3), G7–G17.

Nocedal, J. & Wright, S., 2006. *Numerical optimization*, Springer Science & Business Media.

Operto, S., Virieux, J., Ribodetti, A., & Anderson, J. E., 2009. Finite-difference frequency-domain modeling of viscoacoustic wave propagation in 2D tilted transversely isotropic (TTI) media 2D acoustic wave modeling in TTI media, *Geophysics*, **74**(5), T75–T95.

Paige, C. C. & Saunders, M. A., 1982. LSQR: An algorithm for sparse linear equations and sparse least squares, *ACM Transactions on Mathematical Software (TOMS)*, **8**(1), 43–71.

Patzer, C., 2019. *Time-lapse inversion of Controlled Source Electromagnetics using vertical sources and receivers*, Ph.D. thesis.

Peacock, J. R., Thiel, S., Heinson, G. S., & Reid, P., 2013. Time-lapse magnetotelluric monitoring of an enhanced geothermal system, *Geophysics*, **78**(3), B121–B130.

Plessix, R.-E. & Mulder, W., 2008. Resistivity imaging with controlled-source electromagnetic data: depth and data weighting, *Inverse problems*, **24**(3), 034012.

Puzyrev, V., Koric, S., & Wilkin, S., 2016. Evaluation of parallel direct sparse linear solvers in electromagnetic geophysical problems, *Computers & Geosciences*, **89**, 79–87.

Reinsch, T., 2016. Physical properties of rock at reservoir conditions, IMAGE report FP7, IMAGE, Reykjanes.

Rosas-Carbajal, M., Linde, N., Peacock, J., Zyserman, F. I., Kalscheuer, T., & Thiel, S., 2015. Probabilistic 3-d time-lapse inversion of magnetotelluric data: application to an enhanced geothermal system, *Geophysical Supplements to the Monthly Notices of the Royal Astronomical Society*, **203**(3), 1946–1960.

Routh, P., Palacharla, G., Chikichev, I., & Lazaratos, S., 2012. Full wavefield inversion of time-lapse data for improved imaging and reservoir characterization, in *SEG Technical Program Expanded Abstracts 2012*, pp. 1–6, Society of Exploration Geophysicists.

Shantsev, D. V. & Maaø, F. A., 2015. Rigorous interpolation near tilted interfaces in 3-D finite-difference EM modelling, *Geophysical Journal International*, **200**(2), 745–757.

Shantsev, D. V., Jaysaval, P., De La Kethulle De Ryhove, S., Amestoy, P. R., Buttari, A., l'Excellent, J.-Y., & Mary, T., 2017. Large-scale 3-D EM modelling with a Block Low-Rank multifrontal direct solver, *Geophysical Journal International*, **209**(3), 1558–1571.

Streich, R., 2009. 3D finite-difference frequency-domain modeling of controlled-source electromagnetic data: Direct solution and optimization for high accuracy, *Geophysics*, **74**(5), F95–F105.

Tao, Y., Sen, M. K., Zhang, R., & Spikes, K. T., 2013. A new stochastic inversion workflow for time-lapse data: hybrid starting model and double-difference inversion, *Journal of Geophysics and Engineering*, **10**(3), 035011.

Tietze, K., Ritter, O., & Veeken, P., 2015. Controlled-source electromagnetic monitoring of reservoir oil

saturation using a novel borehole-to-surface configuration, *Geophysical Prospecting*, **63**(6), 1468–1490.

Tietze, K., Ritter, O., Patzer, C., Veeken, P., & Dillen, M., 2019. Repeatability of land-based controlled-source electromagnetic measurements in industrialized areas and including vertical electric fields, *Geophysical Journal International*, **218**(3), 1552–1571.

Wirianto, M., Mulder, W., & Slob, E., 2010. A feasibility study of land CSEM reservoir monitoring in a complex 3-D model, *Geophysical Journal International*, **181**(2), 741–755.

Zhang, Z. & Huang, L., 2013. Double-difference elastic-waveform inversion with prior information for time-lapse monitoring, *Geophysics*, **78**(6), R259–R273.

APPENDIX A: MODELLING AND INVERSION GRID

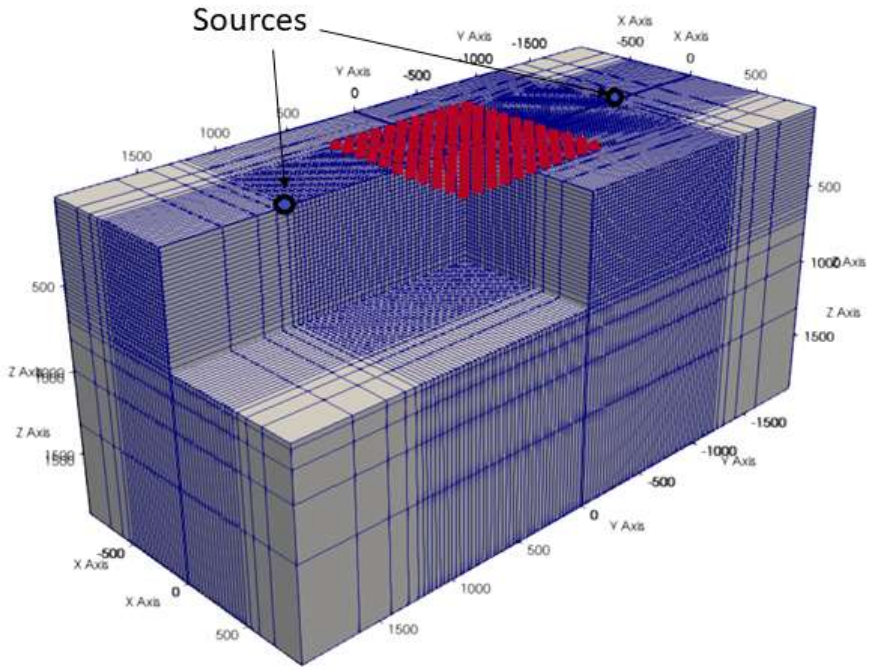

Figure A1. Entire survey layout for synthetic tests with receivers (red dots) and sources (black circles). Modeling grid is display along the three directions.

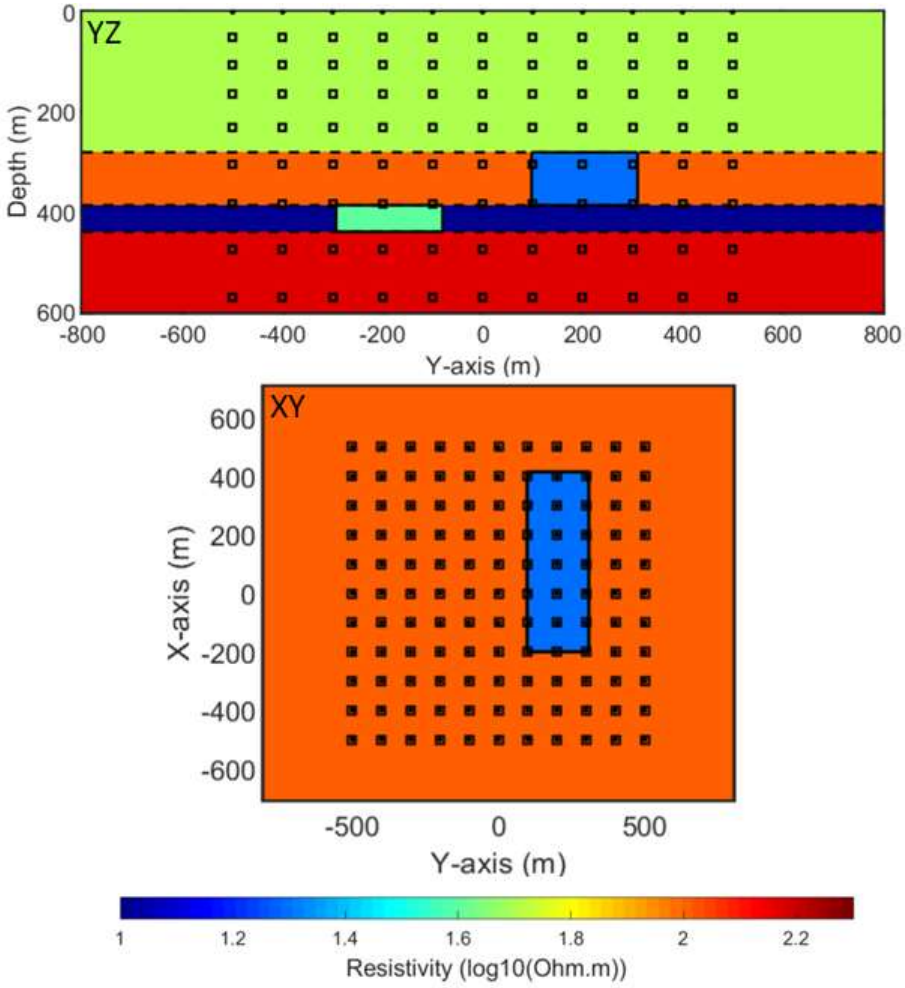

Figure A2. Vertical and horizontal slices of the true model with nodes used for the inversion. These nodes are supports for the B-cubic splines used for parametrization in the inversion.